ECCOMAS Congress 2016
VII European Congress on Computational Methods in Applied Sciences and Engineering
M. Papadrakakis, V. Papadopoulos, G. Stefanou, V. Plevris (eds.)
Crete Island, Greece, 5–10 June 2016

OPTIMAL DESIGN AND ADDITIVE MANUFACTURING OF NOVEL REINFORCING ELEMENTS FOR COMPOSITE MATERIALS

F. Fabbrocino[1], I. Farina[1,2], A. Amendola[3], L Feo[3], F.Fraternali[3]

[1]Pegaso University
Department of Engineering
Piazza Trieste e Trento, 48, 80132 Naples, Italy
francesco.fabbrocino@unipegaso.it

[2]University of Naples Parthenope
Department of Engineering
Centro Direzionale di Napoli, isola C4, 80143- Naples, Italy
ylenia.farina@gmail.com

[3]University of Salerno
Department of Civil Engineering
Via Giovanni Paolo II, 132, 84084 Fisciano, SA, Italy
adamendola@gmail.com, l.feo@unisa.it, f.fraternali@unisa.it

Keywords: Fibres, Fibre/matrix bond, Fracture toughness, Surface analysis, Additive manufacturing

Abstract. *We experimentally investigate on the use of additive manufacturing technologies for the design and fabrication of innovative reinforcing elements of novel composite materials. We perform short-beam shear tests on cement mortar specimens reinforced with additively manufactured reinforcing fibers made of photopolymers or a titanium alloy. The fracture toughness, shear capacity and first crack strength of the examined materials are estimated based on the provisions of different international standards for construction materials. We also characterize the surface morphology of the examined fibers through microscopy analyses before and after testing. The given results highlight that the microscopic or macroscopic nature of the surface roughness of the analyzed fibers greatly influences the energy absorption capacity of the final materials, while the nature of the fibers' material (metallic/polymeric) is of central importance in terms of strength properties. The present study represents a first step in the direction of designing reinforcing elements with hierarchical structure to form fabrics, fibers and coatings of groundbreaking reinforcements for next generation composites, profiting from the rapid prototyping capabilities of additive manufacturing technologies at different scales.*

1 INTRODUCTION

The nascent field of structural "metamaterials", i.e. artificial materials showing unconventional properties mainly derived by their geometric design is growing rapidly and attracting increasing attention from many research areas (refer, e.g., to [1] and references therein). In recent years, additive manufacturing (AM) has become the most common technique for fabricating materials that exhibit unusual behaviors, which are not found in natural materials. Several additive manufacturing methods have been proposed in this field, with resolution ranging from the centimeter- to the nanometer-scale. Worth mentioning here are: polyjet 3D printing technologies; electron beam melting; x-ray lithography; deep ultraviolet lithography; soft lithography; two-photon polymerization; atomic layer deposition; and projection micro-stereolithography, among other available methods (refer to [2][3][4][5][6] and references therein). However, the potential of rapid prototyping in the design of novel mechanical metamaterials is not completely understood at present, and there is an urgent need for research exploring the suitability of such techniques for the manufacture of real life engineering materials.

Most natural shapes exhibit hierarchical organization of matter and fractal geometries, which provide increased surface area for the same volume of material. Recent studies have shown that hierarchical composites showing multiscale fibers coated with carbon nanotubes feature enhanced interlaminar shear strength (ILSS), a key property of composite materials, which can be weak in the presence of smooth matrix-fiber interfaces [7][8]. In such materials, the development of rough fracture surfaces near to the surface of the reinforcing elements, along with crack deflection mechanisms, enhances matrix toughness. The increase in the surface roughness of the reinforcing elements, as compared to smooth interfaces, delays the matrix failure and improves surface energy dissipation [7]. In addition, the pull-out of fine-scale features of the reinforcements bridges the matrix, significantly contributing to the enhancement of composite strength and toughness [8].

The present study investigates the use of additively manufactured reinforcing elements with multiscale geometry for the reinforcement of cementitious mortars. Fibers with structural hierarchy originating from their geometric design are manufactured from computer-aided design (CAD) data, employing additive manufacturing techniques based on polymeric and metallic materials. A first source of hierarchical architecture arises from using fibers covered by lattices on a smaller scale [9]. A second strategy employs meshes with fractal geometry (Figure 1) [10]. Reinforcements with hierarchical structure are combined with a cement mortar, in order to obtain advanced composites with enhanced ILSS, and enhanced first-crack strength and fracture toughness.

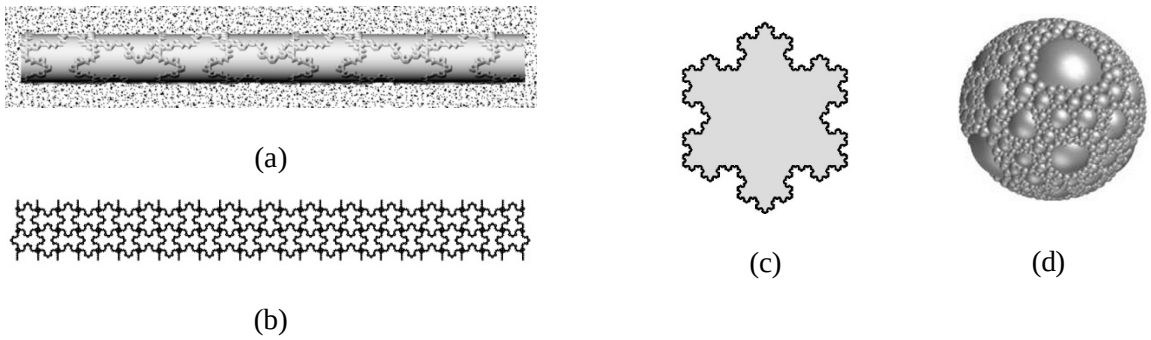

Figure 1: Lattices with fractal geometry used to form reinforcements of composite materials: (a) fiber coating; (b) fabric; (c) fiber cross-section; (d) junction element/fiber embossment (Apollonian sphere packing) [10].

We begin in Sect. 2 by describing the preparation of the mortar and fibers analyzed in the present study. Next, we analyze the first-crack strength and toughness of fiber-reinforced mortar specimens through three point bending tests (Sect. 3). We continue by analyzing the morphology of the fibers' surface in the virgin state and after their pull-out from the matrix (Sect. 4). We end in Sect. 5 with concluding remarks and an outline of future work to be carried out to deepen the potential of AM for the optimal design of novel composite materials.

2 CEMENT MORTAR REINFORCEMENT WITH 3D PRINTED FIBERS

Let us examine the fiber reinforcement of a pre-mixed cement-based mortar matrix of class M5 [11] with mechanical properties shown in Table 1. We employ reinforcing fibers fabricated through two different AM technologies: PolyJet 3D printing of liquid photopolymers through the Objet500 Connex commercial printer by Stratasys®, and electron beam melting (EBM) of high-strength metallic materials through the Arcam EBM S12 facility available at the Department of Materials Science and Engineering of the University of Sheffield.

We printed six polymeric fibers in the photopolymer transparent resin Fullcure 720 (see Table 1 for mechanical properties), with 7.5 mm diameter and 100 mm length, Three of these fibers show smooth lateral surface (hereafter denoted as "Pol_S" fibers, see Figure 2a), while another three are coated on the lateral surface with a fractal lattice based on the Koch snowflake ("Pol_R" fibers, see Figure 1a and Figure 2b).

Metallic fibers were also produced, employing EBM to manufacture four cylindrical fibers in the titanium alloy Ti6Al4V [6], with 7.5 mm diameter, 160 mm length, and smooth lateral surface ("Ti_S" fibers, see Figure 3a,c and). We also employed EBM to produce four 7.0 mm diameter Ti6Al4V fibers, coated with a 0.75 mm × 0.75 mm grid of cylindrical embossments. These cylinders exhibit 0.20 mm diameter and 0.50 mm length ("Ti_R" fibers, see Figure 3b,d and Figure 4: Cross-section (a) and 3D view (b) of a portion of the Ti_R fiber).

A microscope characterization of the surface morphology of the examined fibers is given in Sect. 4. Such fibers were employed to reinforce prismatic specimens of a cement mortar with square cross-section, 40 mm width and 160 mm length. Mortar specimens were manufactured by adding 180 cc of water for each kg of the pre-mixed cement mortar, according to manufacturer's recommendations. We set the mortar cover of Pol_S and Pol_2 fibers equal to 20 mm (effective depth equal to 200 mm: fibers placed at mid-height), and that of Ti_S and Ti_R fibers equal to 7 mm (effective depth equal to 33 mm). The above fiber placements were aimed at reproducing pure crack-bridging reinforcement in the case of the low modulus Pol_S and Pol_R fibers, and combined shear-flexure reinforcement in the case of the high modulus Ti_S and Ti_R fibers (see Table 1). All the specimens were cured at room temperature for 28 days before testing. We use the nomenclature Pol_R, Pol_S, Ti_R, and Ti_S to denote the mortar specimens reinforced with the corresponding 3D printed fibers, and unreinforced mortar specimens by the symbol UNR. We manufactured three Pol_R, Pol_S, Ti_R and Ti_S specimens each, and four UNR specimens.

(a)

(b)

Figure 2: Photographs of Pol_S (a) and Pol_R (b) fibers.

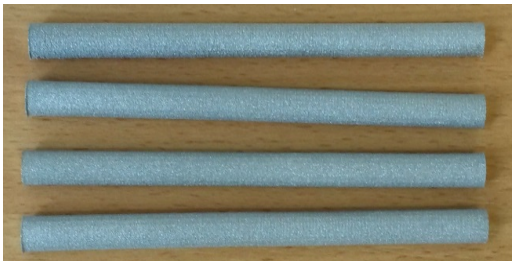

(a)

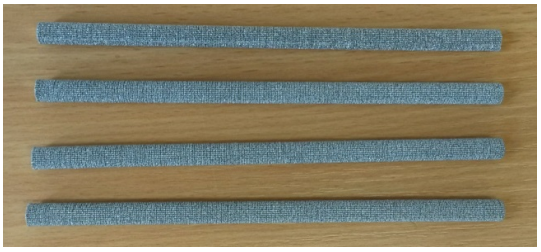

(b)

(c)

(d)

Figure 3: Top and side views of Ti_S (a,c) and Ti_R (b,d) fibers.

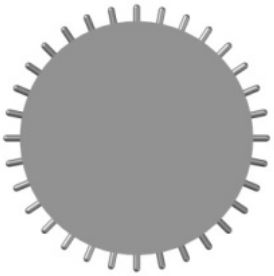

(a)

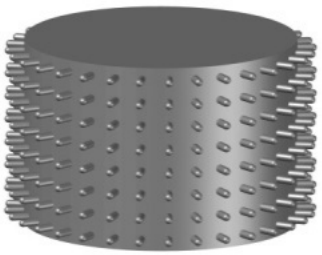

(b)

Figure 4: Cross-section (a) and 3D view (b) of a portion of the Ti_R fiber.

Class M5 mortar	
mass density [kg/m^3]	1515
compressive strength [MPa]	5
flexural strength [MPa]	1
Fullcure 720 Stratasys® photopolymer	
mass density [kg/m^3]	1.18-1.19
tensile strength [MPa]	50-65
modulus of elasticity [MPa]	2000-3000
Ti6Al4V titanium alloy	
mass density [kg/m^3]	4430
tensile strength [MPa]	950
modulus of elasticity [GPa]	120

Table 1: Mechanical properties of mortar and fibers.

3 THREE POINT BENDING TESTS

We studied the mechanical response of the examined fiber-reinforced mortars by carrying out three- point bending (TPB) tests in displacements control, with 0.25 mm/min loading rate. For each examined specimen, we first determined the applied load versus mid-span deflection curve, and next we computed the first crack strength, shear capacity and material toughness according to the methods specified in the international standards for construction materials. The load-deflection curves obtained for Pol_S and Pol_R specimens are illustrated in Figure 5 and Figure 6, respectively, while the analogous curves competing to Ti_S and Ti_R specimens are given in Figure 7 and Figure 8, respectively. Figure 9- Figure 11 illustrate the synchronization of frames taken from in-situ videos of the TPB tests and the load-deflection curve of some Pol_R, Ti_S and Ti_S specimens [12]. Finally, Figure 12 provides pictures of the configurations after TPB testing of selected specimens.

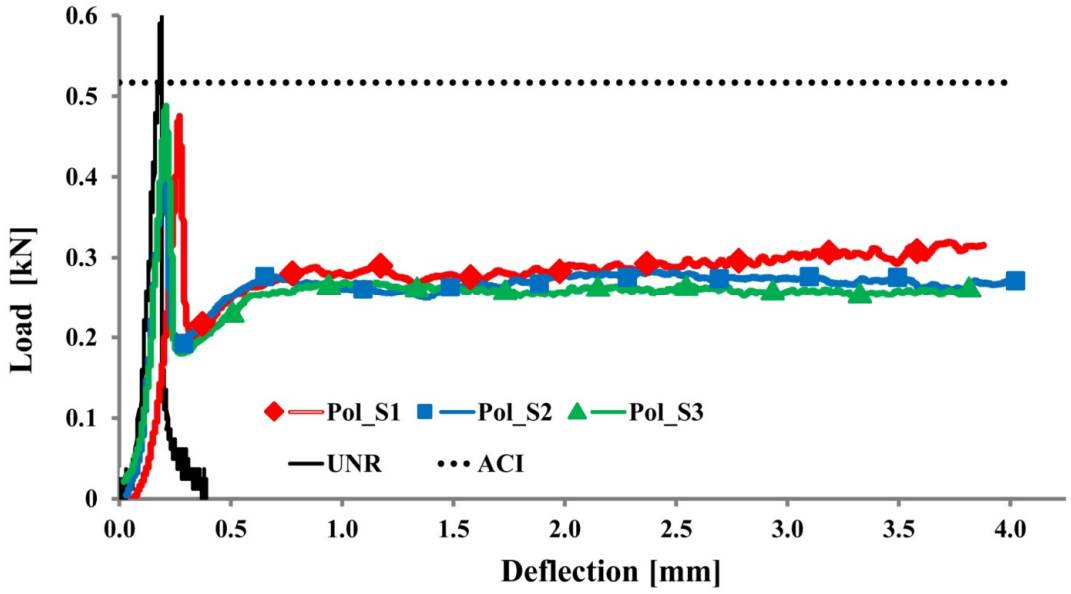

Figure 5: Force vs. deflection curves of Pol_S specimens (UNR: averaged response of UNR specimens).

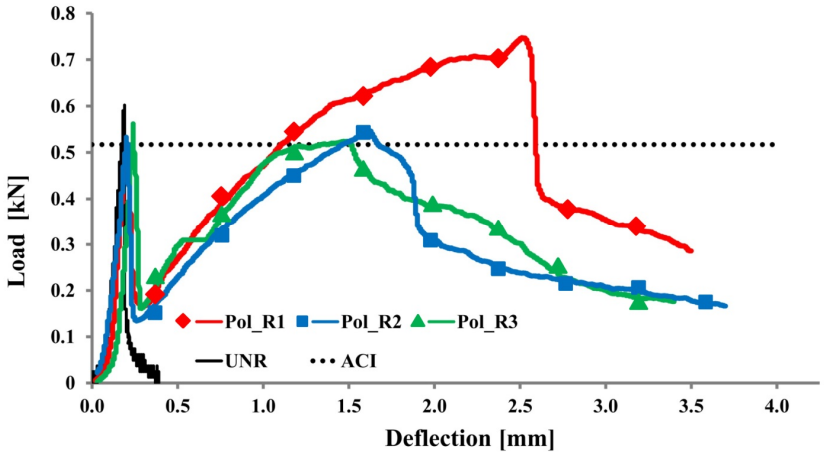

Figure 6: Force vs. deflection of Pol_R specimens (UNR: averaged response of UNR specimens).

The results in Figure 5 and Figure 6 highlight that the maximum load carried by UNR specimens is approximatively equal to 0.6 kN, and is reached just before crack onset. Such specimens exhibit brittle failure, and fast snapping to a collapsed configuration with zero residual strength after crack onset (see Fig. 12a). In contrast to this, Pol_S specimens exhibit residual load carrying capacity approximately constant and equal to 0.25 kN in the post-cracking regime (Figure 5). The load-deflection curves of Pol_R specimens show a marked load drop after crack onset, which is followed by a hardening branch, and next by a second load drop and a softening branch leading to specimen failure (Figure 6). In such specimens, we observed a shear-type failure affected by diagonal cracks propagating from the point of application of the vertical load (see Figure 9 and Fig. 12c), while in Pol_S specimens we observed a flexural-type failure due to the vertical propagation of the central crack up to failure (no diagonal cracks, see Fig. 12b).
Figure 7 and Figure 8 illustrate the results of TPB tests on Ti_S and Ti_R specimens, respectively. Both Ti_S and Ti_R specimens show force-deflection response characterized by a load drop at crack onset; a slightly hardening response after such a load drop; a second load drop and a final plateau or softening branch leading to specimen failure.

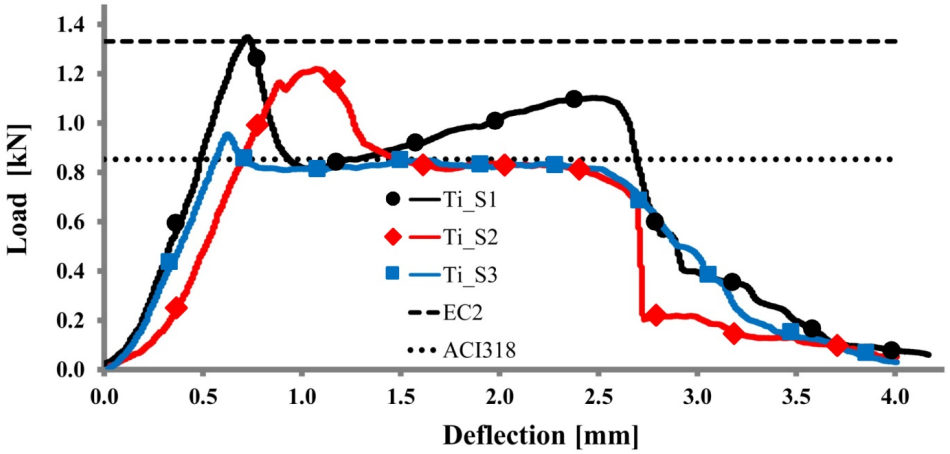

Figure 7: Force vs. deflection curves of Ti_S specimens.

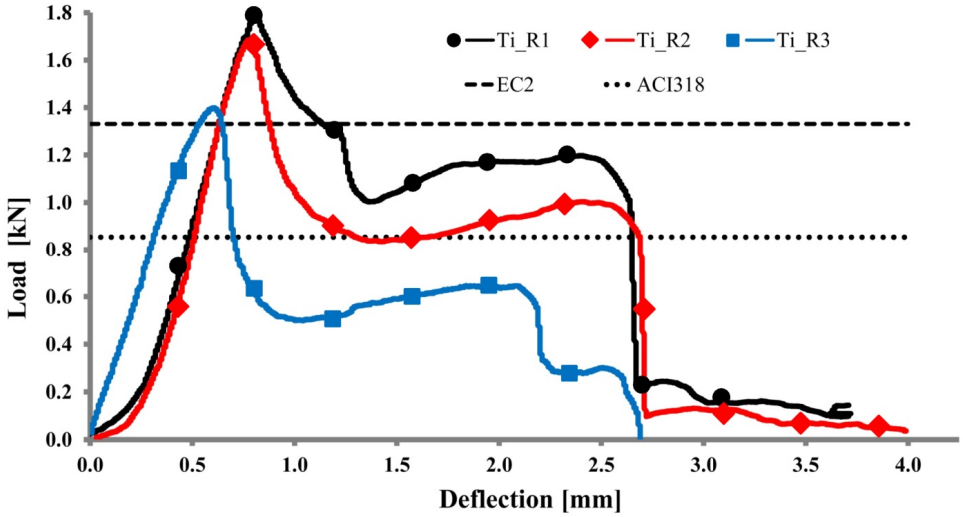

Figure 8: Force vs. deflection curves of Ti_R specimens.

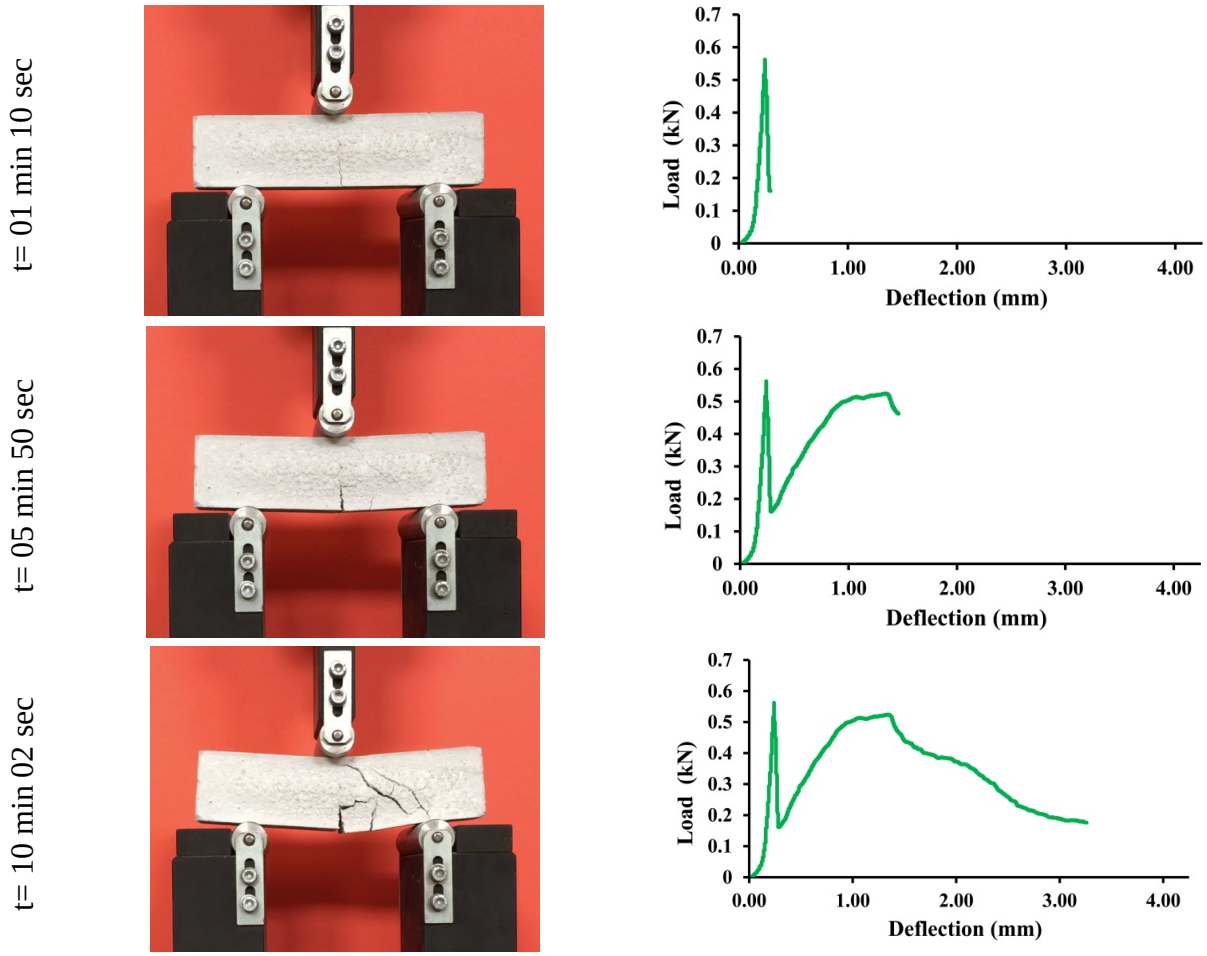

Figure 9: Synchronization between frames from an in-situ video of a TPB on the Pol_R specimen #3 (left) and the load-deflection curve of the same specimen (right).

The maximum load carried by Ti_S specimen (at crack opening) is about equal to 1.1 kN on average (Figure 7), while the maximum load carried by Ti_R specimens is about equal to 1.6 kN on average (Figure 8). It is worth noting that both Ti_S and Ti_R specimens exhibit maximum load carrying capacity that is more than twice that of Pol_S (~0.45 kN, cf. Figure 5), Pol_R (~0.55 kN, cf. Figure 6) and UNR (~0.60 kN, cf. Figure 5-Figure 6) specimens. Both Ti_S and Ti_R specimens exhibited shear-type failure, as shown in Figure 10, Figure 11, and Figure 12d-e. The optical microscopy analyses presented in Sect. 4 show that Ti_S fibers exhibit considerable surface roughness (not included in the CAD design), as well as Ti_R fibers, due to material processing defects (like, e.g., internal porosity) common in the EBM process [6].

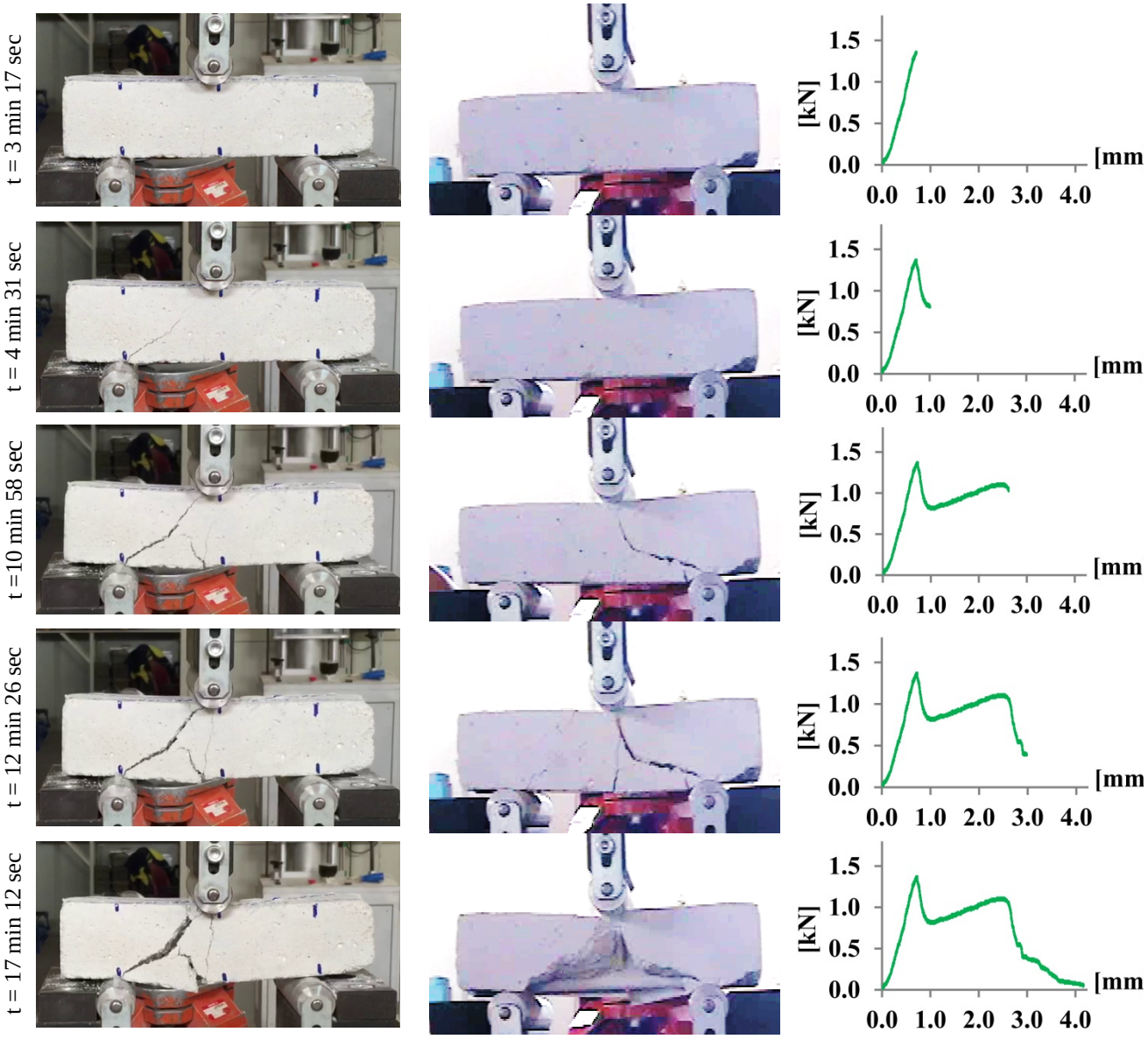

Figure 10: Synchronization of frames from in-situ videos of a TPB on the Ti_S specimen #1 (left: front view, center: back view) and the load-deflection curve of the same specimen (right).

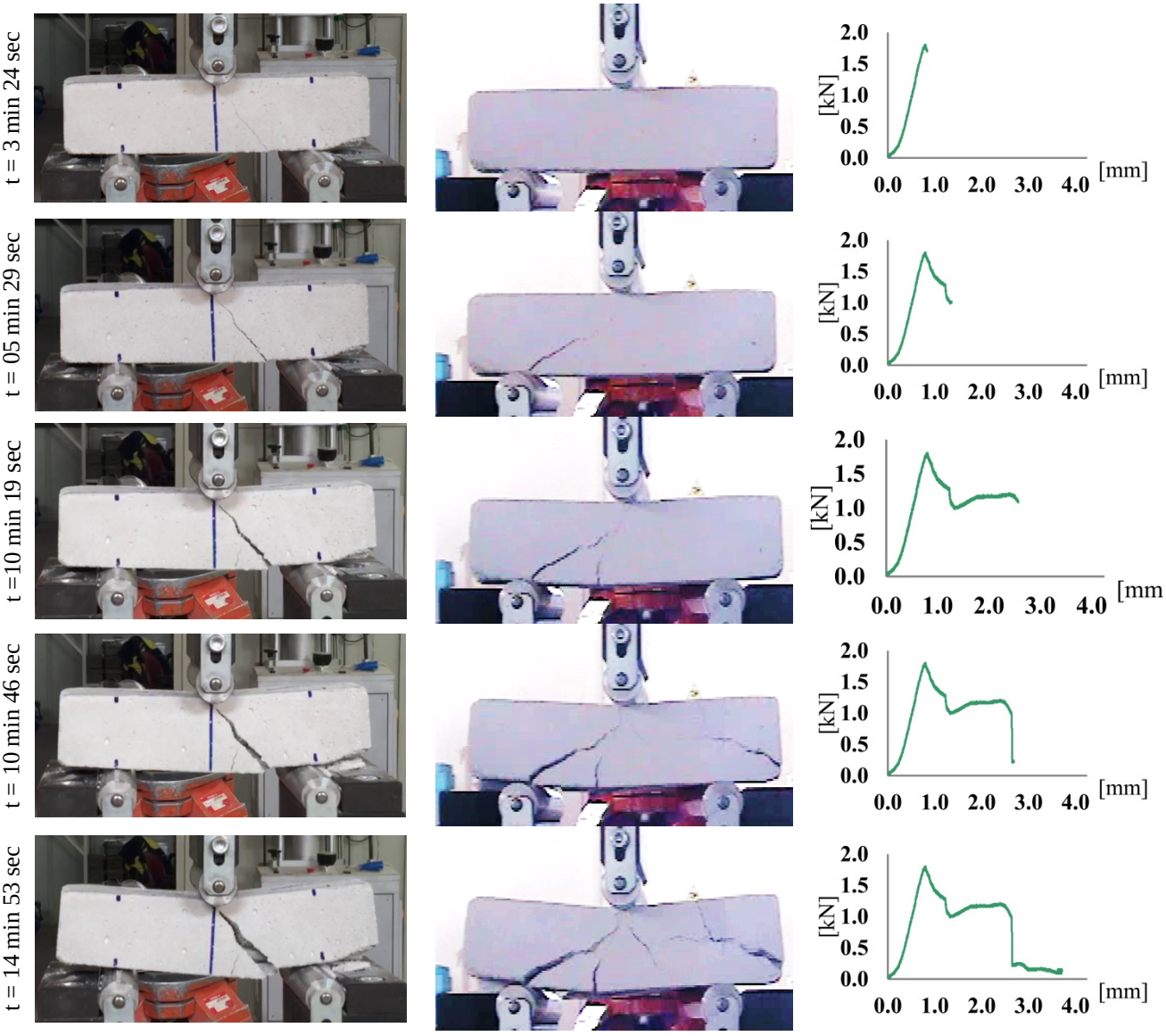

Figure 11: Synchronization of frames from in-situ videos of a TPB on the Ti_R specimen #1 (left: front view, center: back view) and the load-deflection curve of the same specimen (right).

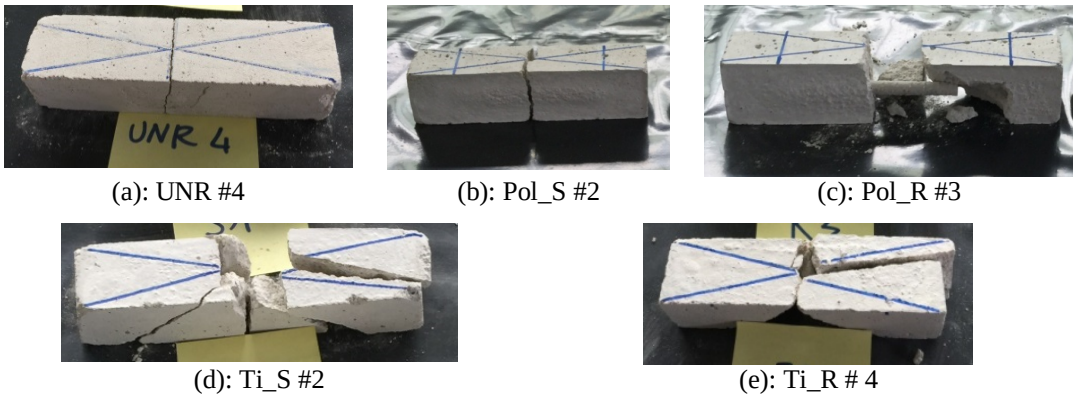

(a): UNR #4 (b): Pol_S #2 (c): Pol_R #3

(d): Ti_S #2 (e): Ti_R # 4

Figure 12: Pictures of different specimens taken after the completion of TPB tests.

3.1 Fracture toughness

By extending the provisions of ASTM C1018 [13] to the current materials, we characterize the fracture toughness of the fiber-reinforced mortars examined in the present study through the following index:

$$I = \frac{A\left(\delta = 3\bar{\delta}\right)}{A_{UNR}\left(\bar{\delta}\right)}, \tag{1}$$

where $\bar{\delta}$ denotes the mid-span deflection in correspondence with the first crack load of the generic specimen; $A\left(\delta = 3\bar{\delta}\right)$ denotes the area under the load-deflection curve from the origin up to $\delta = 3\bar{\delta}$; and $A_{UNR}\left(\bar{\delta}\right)$ denotes the mean value of the area under the load-deflection curve of UNR specimens up to crack opening. The above index represents a measure of the relative energy absorption capacity of the fiber-reinforced materials against the unreinforced mortar. Table 2 gives the toughness index I of the examined mortar specimens, and the mean values of such a quantity that we recorded for each different material.

specimen	I	mean value		specimen	I	mean value
Pol_S_1	3.12	3.12		Ti_S_1	39.08	41.63
Pol_S_2	3.24			Ti_S_2	51.59	
Pol_S_3	3.01			Ti_S_3	34.23	
Pol_R_1	2.36	2.87		Ti_R_1	68.15	51.15
Pol_R_2	3.13			Ti_R_2	52.87	
Pol_R_3	3.12			Ti_R_3	32.44	

Table 2: Fracture toughness indices of the examined specimens.

The results in Table 2 show that Pol_S and Pol_R specimens exhibit a considerable energy absorption capacity, as compared to unreinforced specimens, while Ti_S and Ti_R specimens exhibit extremely large values of I, as compared both to the unreinforced mortar analyzed in the present study, and the fiber reinforced mortars and concretes analyzed in [14][15][16][17][18][19][20]. It is worth noting, however, that most of specimens analyzed in the present work exhibit flexural collapse under deflections lower than $5.5\,\bar{\delta}$, which make it impossible to compute the toughness index I_{10} and the residual strength factor $R_{5,10}$ [14][15] for such materials. In other words, the materials examined in the present study exhibit large toughness and residual strength in the first post-crack regime [16][17], but brittle response for very large deflections (increased brittleness in additively manufactured Ti6Al4V is frequently observed at high strains, due to the low defect tolerance of the alloy [21]). We remark, however, that the deflection regime $\delta \le 3\bar{\delta}$ characterizes a wide range of real-life applications dealing with small or moderately large strains of construction materials.

3.2 Shear capacity and first crack strength

As we already noticed, Pol_R, Ti_S and Ti_R specimens exhibited shear failure under TPB tests, with propagation of diagonal cracks from the point of application of the external load down to the hinge supports (cf. Figure 9-12) [22][23]. On extending results for reinforced concretes without shear reinforcements [22][23] to the present mortars, we hereafter analyze the provisions of different international standards for the shear capacity of such mate-

rials. The shear capacities predicted by ACI 318 [24], BS 8110-1[25], and EC2 [26] are respectively given by the following formulas

$$V_{Rd}^{ACI} = 0.17\phi_c \sqrt{f_{ck}}\, bd \tag{2}$$

$$V_{Rd}^{BS} = \frac{0.79}{\gamma_M}\left(100\frac{A_s}{bd}\right)^{\frac{1}{3}}\left(\frac{400}{d}\right)^{\frac{1}{4}}\left(\frac{f_{ck}}{25}\right)^{\frac{1}{3}} bd \tag{3}$$

$$V_{Rd}^{EC2} = \min\left\{\frac{0.18}{\gamma_c}k\left(100\frac{A_s}{bd}\, f_{ck}\right)^{1/3},\ 0.035\left(1+\sqrt{\frac{200}{d}}\right)^{\frac{3}{2}}\sqrt{f_{ck}}\right\} bd \tag{4}$$

where: A_s and d are the fiber cross sectional area and the effective depth of the cross-section (cross-section height minus the mortar cover), respectively; f_{ck} denotes the characteristic compressive strength of the mortar declared by the manufacturer ($f_{ck} = 5.00$ MPa, cf. Table 1); and it results: $\gamma_M = 1.25$, $\phi_c = 0.85$, $\gamma_c = 1.5$.

Table 3 compares the predictions of the shear capacities of the examined materials with the mean values of the experimental capacities $\overline{V}_{\exp}$ corresponding to one half of the peak loads observed in Figure 5 - Figure 8 (averaged among all specimens). The results in Table 3 show that ACI 318 [24] best matches experimental results for Pol_R and Pol_S specimens (0.26 kN vs 0.27-0,.30 kN), while EC2 [26] instead best matches the experimental shear capacity of Ti_S and Ti_R specimens (0.67 kN vs 0.65-0.83 kN). It should be remarked that the above codes do not account for the surface microstructure and roughness of the reinforcing elements.

specimens	d	A_s	$\overline{V}_{\exp}$	V_{Rd}^{BS}	V_{Rd}^{ACI}	V_{Rd}^{EC2}	$\bar{f}_{cr}$
	$[mm]$	$[mm^2]$	$[kN]$	$[kN]$	$[kN]$	$[kN]$	$[MPa]$
Pol_S	20	44.18	0.27	0.79	0.26	0.53	1.25
Pol_R	20	44.18	0.30	0.79	0.26	0.53	1.42
Ti_S	33	38.48	0.65	1.15	0.42	0.67	1.45
Ti_R	33	38.48	0.83	1.15	0.42	0.67	1.97

Table 3: Comparison between experimental and theoretical predictions of shear capacity and first crack strength.

We now investigate on the first crack strength of the analyzed materials by computing the maximum tensile stress f_{cr} carried by the mortar in correspondence with the load F_{cr} that produces crack initiation. The bending moment associated with such a load is trivially equal to $M_{cr} = F_{cr}L/4$, L denoting the clear length of the specimen ($L = 100\ mm$). On assuming linear elastic behavior of the material up to crack initiation and homogenized properties for the fiber-reinforced cross-section [26], we obtain the mean values of f_{cr} given in Table 3. Such results correspond to assuming the fiber-mortar homogenization factor equal to E_f / E_m, where E_f is the Young modulus of the fiber material (see Table 1), and E_m is the Young modulus of the mortar. The latter has been computed as $E_m \cong 1000\, f_{ck}$ [27], obtaining: $E_m \sim 5000$ MPa. The results in Table 3 show that all the fiber reinforced specimens exhibit first crack strength greater than the flexural strength of the mortar declared by the manufac-

turer (1.0 MPa, cf. cf. Table 1). The maximum value of such a property is exhibited by Ti_R specimens, (1.97 MPa), which is considerably larger than the first crack strength of Ti_S (1.45 MPa), Pol_S (1.25 MPa) and Pol_R (1.42 MPa) specimens.

4 SURFACE MORPHOLOGY OF 3D PRINTED FIBERS BEFORE AND AFTER TESTING

Optical microscopy was employed to investigate on the morphology of the fiber surface at the virgin state and after their pull-out from the matrix. Figure 12 shows optimal microscope images of the examined fibers taken with the optical microscope Olympus SZ-PT using 1500× magnification, before their insertion into the matrix (a), and after fiber pull-out (b). Grayscale versions of the images in Figure 12 were obtained through ImageJ (http://imagej.nih.gov/ij/), a public domain Java image processing software. Each image in Figure 12 was captured and converted from color to grayscale, by application of a grey value threshold and elliptical fit (Figure 13).

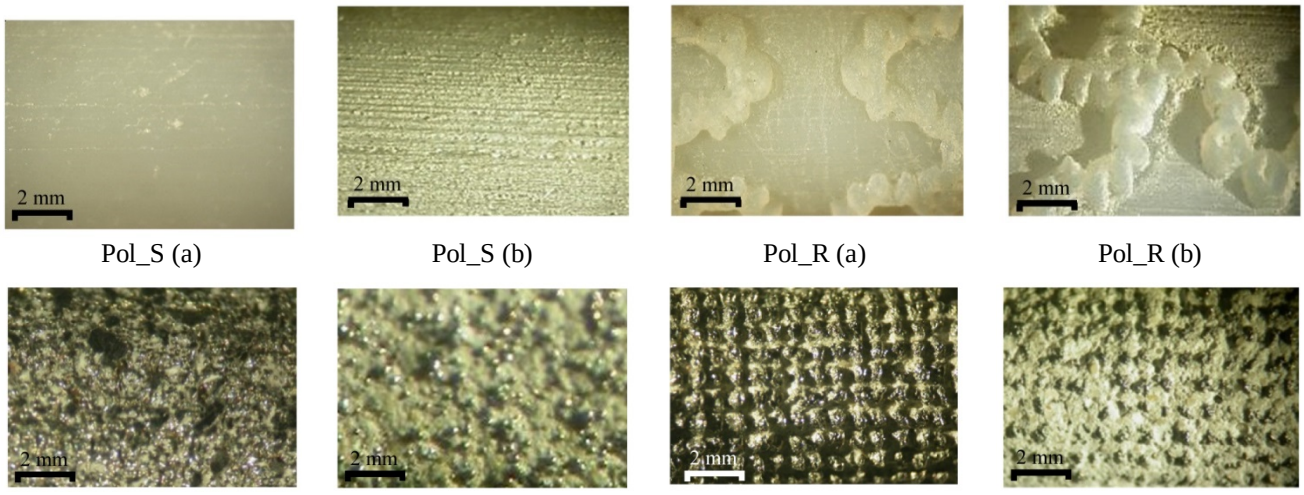

Figure 12: Optical microscope images (1500× magnification).of the examined fibers before test (a) and after pull-out (b).

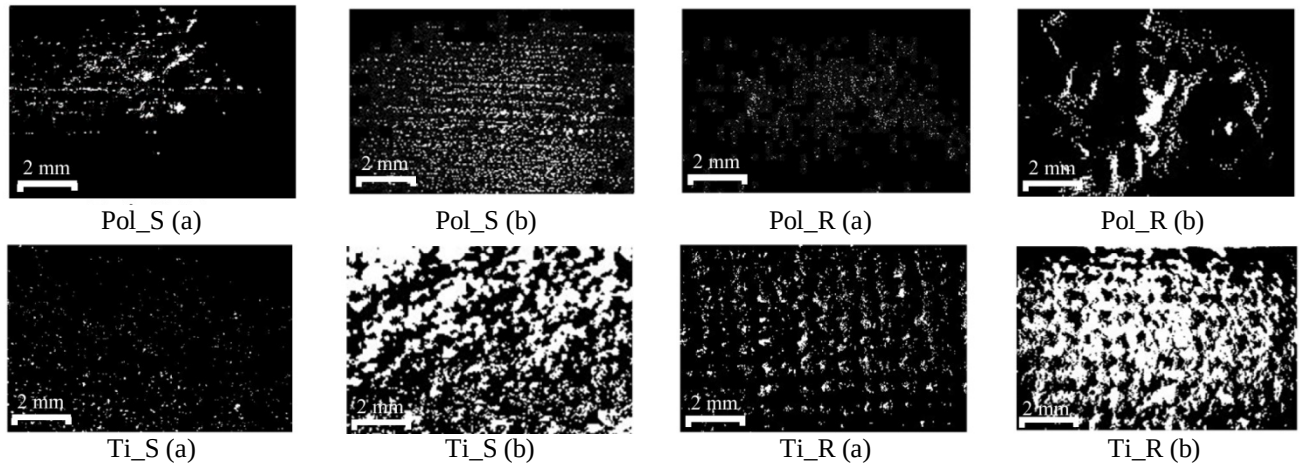

Figure 13: Grayscale images of the examined fibers before test (a) and after pull-out (b).

The images provided in Figure 12-Figure 13 show the presence of mortar particles attached to the pulled-out fibers. Large size mortar particles (with maximum features up to ~1.0 mm) are

visible on the surface of Ti_R and Pol_R fibers, while finer scale particles are visible on the surface of the Ti_S fiber. Small size mortar particles are also visible on the surface of the Pol_S fiber after pull-out. The presence of large size mortar particles attached to the pulled-out fibers is an indicator of high roughness of the fracture surface at the fiber-matrix interface. Such a phenomenon proves that a layer of matrix covers the fiber during the pull-out, causing enhanced interfacial bonding. The development of a rough fracture surface within such a layer, and the crack-deflection mechanisms observed in Figure 9-Figure 11 indicate improvement of matrix toughness in presence of shear failure. Overall, we observe significant increases in the interlaminar shear strength of mortars reinforced with Pol_R, Ti_S and Ti_R fibers, as compared to the unreinforced material.

5 CONCLUDING REMARKS

We have investigated the use of 3D printed fibers for the flexural reinforcement of a cement mortar, employing polymeric (Fullcure 720 Stratasys® photopolymer) and metallic (Ti6Al4V titanium alloy) fibers manufactured with different technologies and surface morphologies.

Three point bending tests on fiber-reinforced mortar specimens have highlighted crack patterns indicating shear failure in the case of reinforcements with high surface roughness fibers (Pol_R, Ti_S and Ti_R fibers), and flexural failure in the case of reinforcements with smooth (Pol_S) fibers, as well as in the case of unreinforced specimens (Sect. 3). The results of Sect. 4 show that the fiber surface geometry strongly influences interfacial bonding, while the chemical nature of the fiber and mortar materials markedly affects the shear capacity and the flexural strength of the fiber-reinforced material (cf. Sect. 3.2).

All the results presented in this study indicate that an optimized fiber surface design may significantly increase the energy absorption capacity of fiber-reinforced mortars. They represent a first step in the direction of designing reinforcing elements with hierarchical structure to form fabrics, fibers and coatings of groundbreaking reinforcements for next generation composites, profiting from the rapid prototyping capabilities of AM technologies at different scales.

Future extensions of the present study (see, e.g., [28]) will focus on nano-, micro- and macro-scale lattice reinforcements for a wide range composite materials, through a closed-loop approach including the computational design and the additive manufacturing of physical models via innovative, multimaterial deposition techniques. Such materials will be used, e.g., for the fabrication of innovative materials, and the structural retrofitting of existing buildings and historical constructions [29][30][31][32].

An experimental characterization phase will implement and verify the theoretical predictions. The design phase will employ multiscale approaches to the toughness and strength of composite materials reinforced with multiscale fibers and/or fabrics, as a function of the microstructure [33][34]. Mechanical models of the composite material will be formulated at the meso-scale, through discrete and/or finite element approaches, assuming different constitutive equations for the bulk phases and the reinforcement-matrix interface (via variational fracture [34][35]). The optimal topologies of the reinforcing elements will be researched using structural optimization procedures [36][37][38], on employing minimum weight, maximum composite strength, and/or maximum fracture toughness as goal functions.

REFERENCES

[1] M.H. Lu, L. Feng, Y.F. Chen, Phononic crystals and acoustic metamaterials. *Materials. Today*. 12, 34-42, 2009.

[2] M. Kadic, T. Bückmann, N. Stenger, M. Thiel, M. Wegener, On the practicability of pentamode mechanical metamaterials. *Applied Physics Letters,*100, 191-901, 2012.

[3] M. Schittny, T. Bückmann, M. Kadic, M. Wegener, Elastic measurements on macroscopic three-dimensional pentamode metamaterials. *Applied Physics Letters,*103, art. no. 231905, 2013.

[4] L.R. Meza, S. Das, J.R. Greer. Strong, lightweight, and recoverable three-dimensional ceramic nanolattices, *Science*, 345, 1322-26, 2014.

[5] Zheng X et al. Design and optimization of a light-emitting diode projection micro-stereolithography three-dimensional manufacturing system. *Review of Scientific Instruments*, 83, art. no. 125001, 2012.

[6] A. Amendola, E.H. Nava, R. Goodall, I. Todd, R.E. Skelton, F. Fraternali. On the additive manufacturing and testing of tensegrity structures, *Composite Structures*, 131, 66-71, 2015.

[7] J. Li, Z. Wu, C. Huang, L. Li. Multiscale carbon nanotube-woven glass fiber reinforced cyanate ester/epoxy composites for enhanced mechanical and thermal properties. *Composite Science and Technology*, 104, 81-88, 2014.

[8] H. Mei, Q. Bai, T. Ji, H. Li, L. Cheng. Effect of carbon nanotubes electrophoretically-deposited on reinforcing carbon fibers on the strength and toughness of C/SiC composites. *Composite Science and Technology*. 103, 94-99, 2014.

[9] N.A. Fleck, V.S. Deshpande, M.F. Ashby, Micro-architectured materials: past, present and future, *Proceedings of the Royal Society of London A: Mathematical, Physical and Engineering Sciences.*,466, 2495–516, 2010.

[10] F. Fraternali, F. Fabbrocino, I. Farina. *Multiscale Structural Element ("Elemento Strutturale a Geometria Multiscala"*) Italian Patent Application No.102015000044896, (http://www.fernandofraternaliresearch.com/publications/P1115IT00_Brevetto_Elemento_Multiscala_2015.pdf, accessed on Oct. 28, 2015).

[11] EN 998-2, 2003. *Specification for mortar for masonry - Part 2: Masonry mortar*.

[12] J.R. Raney, F. Fraternali, A. Amendola, C. Daraio. Modeling and in situ identification of material parameters for layered structures based on carbon nanotube arrays. *Composite Structures*, 93, 3013–18, 2011.

[13] ASTM C1018. *American Society for Testing and Materials. Standard test method for flexural strength of fiber reinforced concrete.* Book of ASTM Standards. Barr Harbor Drive (West Conshohocken, PA, United States): ASTM; 1998.

[14] F. Fraternali, I. Farina, C. Polzone, E. Pagliuca, L. Feo, On the use of R-PET strips for the reinforcement of cement mortars. *Composites. Part B, Engineering*, 46, 207-10, 2013.

[15] S. Spadea, I. Farina, A. Carrafiello, F. Fraternali, Recycled nylon fibers as cement mortar reinforcement. *Construction and Building Materials*, 80, 200-9, 2015.

[16] F. Fraternali, V. Ciancia, R. Chechile, G. Rizzano, L. Feo, L. Incarnato. Experimental Study of the Thermo-Mechanical Properties of Recycled PET Fiber Reinforced Concrete. *Composite Structures*, 93, 2368–74, 2011.

[17] F. Fraternali, S. Spadea, V.P. Berardi, Effects of recycled PET fibers on the mechanical properties and seawater curing of Portland cement-based concretes. *Construction and Building Materials*, 61, 293-302, 2014.

[18] E. Cuenca, J. Echegaray-Oviedo, . Serna P Influence of concrete matrix and type of fiber on the shear behavior of self-compacting fiber reinforced concrete beams. *Composites. Part B, Engineerin*g,,75, 135-47, 2015.

[19] H. Kim, G. Kim, N. Gucunski, J. Nam, J. Jeon, Assessment of flexural toughness and impact resistance of bundle-type polyamide fiber-reinforced concrete. *Composites. Part B, Engineerin*g,78, 431-46, 2015.

[20] A. Martins, G. Vasconcelos, R. Fangueiro, F. Cunha, Experimental assessment of an innovative strengthening material for brick masonry infills. *Composites. Part B, Engineerin*g, 80, 328-42, 2015.

[21] E. Hernandez-Nava, C.J. Smith, F. Derguti, S. Tammas-Williams, F. Leonard, P.J. Withers, I. Todd, R. Goodall, The effect of density and feature size on mechanical properties of isostructural metallic foams produced by additive manufacturing, Acta Materialia, 85, 387–95, 2015.

[22] G.A. Rombach, M. Kohl, V.H. Nghiep, Shear Design of Concrete Members without Shear Reinforcement - A Solved Problem? *Procedia Engineering*, 14, 134–40, 2011.

[23] T. Ikegawa, H. Saito, H. Ohuchi, H. Kitoh, H. Tsunokake, Flexural and Shear Failure Tests of Reinforced Concrete Beams with Low Grade Recycled Aggregate. *Memoirs of the Faculty of Engineering*, Osaka City University, 50, 29-36, 2009.

[24] ACI Task Committee 318. *Building code requirements for structural concrete (ACI 318-08) and commentary*. American Concrete Institute. Farmington Hills, 2008.

[25] BS8110-1. *Structural use of concrete, part 1: Code of practice for design and construction*. British Standards Institute. London, 1997.

[26] EN 1992-1-1:2004. *Eurocode 2. Design of concrete structures - Part 1-1: General rules and rules for buildings.*

[27] EN 1996-1-1:2005. *Eurocode 6: Design of masonry structures - Part 1-1: General rules for reinforced and unreinforced masonry structures.*

[28] I. Farina, F. Fabbrocino, G. Carpentieri, M. Modano, A. Amendola, R. Goodall, L. Feo, F. Fraternali, On the reinforcement of cement mortars through 3D printed polymeric and metallic fibers. *Composites. Part B, Engineerin*g, 90, 76-85, 2016.

[29] F. Fraternali, G. Carpentieri, M. Modano, F. Fabbrocino, R.E. Skelton, A tensegrity approach to the optimal reinforcement of masonry domes and vaults through fiber-reinforced composite material. *Composite Structures*, 134, 247-54, 2015.

[30] F. Fabbrocino, I. Farina, V.P. Berardi, A.J.M. Ferreira, F. Fraternali, On the thrust surface of unreinforced and FRP-/FRCM-reinforced masonry domes. *Composites. Part B, Engineerin*g, 83, 297-305, 2015.

[31] F. Fraternali, G. Carpentieri, A. Amendola, R.E. Skelton, V.F. Nesterenko, Multiscale tunability of solitary wave dynamics in tensegrity metamaterials, *Applied Physics Letters*, 105 (20), art. no. 201903, 2014.

[32] A. Bossio, F. Fabbrocino, G.P. Lignola, A. Prota, G. Manfredi, Simplified model for strengthening design of beam-column internal joints in Reinforced Concrete Frames, *Polymers*, 7 (9), 1732-1754, E-ISSN: 2073-4360, DOI: 10.3390/polym7091479, 2015.

[33] Y. Li, M. Zhou, Prediction of fracture toughness of ceramic composites as function of microstructure: I. Numerical simulations, *Journal of the Mechanics and Physics of Solids*, 61(2), 472-88, 2013.

[34] F. Fraternali, Free Discontinuity Finite Element Models in Two-Dimensions for In-Plane Crack Problems, *Theoretical and Applied Fracture Mechanics*, 47, 274-82, 2007.

[35] B. Schmidt, F. Fraternali, M, Ortiz, Eigenfracture: An eigendeformation approach to variational fracture. *Multiscale Modeling and Simulation*, 7(3), 1237-66, 2009.

[36] F. Fraternali, A. Marino, T. El Sayed, A. Della Cioppa, On the structural shape optimization through variational methods and evolutionary algorithms. *Mechanics of Advanced Materials and Structures*, 18, 224-43, 2011.

[37] R.E. Skelton, F. Fraternali, G. Carpentieri, A. Micheletti, Minimum mass design of tensegrity bridges with parametric architecture and multiscale complexity. *Mechanics Research Communications*,58, 124-32, 2014.

[38] G. Carpentieri, M. Modano, F. Fabbrocino, F. Fraternali, Optimal design and dynamics of truss bridges, *COMPDYN 2015 - 5th ECCOMAS* Thematic Conference on Computational Methods in Structural Dynamics and Earthquake Engineering, 1731-1740, 2015